ADVANCED OPTICAL MATERIALS
www.advopticalmat.de

# Lattice Strain Enhanced Phase Transformation of $NaYbF_4$: 2% $Er^{3+}$ Upconverting Nanoparticles by Tuning the Molar Ratio of $Na^+/Yb^{3+}$

*Weitong Xiao, Jingyang Chen, Feiran Wang, Weiling Luan,* Yiting Wu, and Lyudmila Turyanska**

**$NaYbF_4$ upconverting nanoparticles (UCNPs) have enhanced optical properties compared to the $NaYF_4$ UCNPs. However, synthesis of monodisperse $NaYbF_4$ with controllable size and optical properties poses challenges, and the mechanism of phase transformation remains to be understood. Here, they report on the effect of $Na^+/Yb^{3+}$ molar ratio on the morphological and optical properties of upconverting $NaYbF_4$: 2% $Er^{3+}$ nanoparticles. Controllable transformation of cubic phase nanoparticles produced with $[Na^+]/[Yb^{3+}] = 1$ to hexagonal phase is achieved by increasing $Na^+$ content. The hexagonal UCNPs produced with $[Na^+]/[Yb^{3+}] = 4$ have significantly enhanced intensity of optical emission of ≈600 times compared with the pure cubic phase crystal. The work reveals that the increasing dislocation of sodium and ytterbium distribution cause the accumulation of the lattice strain with increasing $Na^+$ content, and triggers the lattice strain-mediated phase transformation in cubic cell, as confirmed by the Density Function Theory simulations. These results provide new insights into the growth of UCNPs and pave the way for developing controlled synthesis of UCNPs for applications as bio-probes and for energy harvesting.**

## 1. Introduction

Lanthanide-doped upconverting nanoparticles (UCNPs) have attracted significant interest due to their unique optical performance and stability,[1] and offer advantages for applications ranging from bioimaging to multicolor displays.[2] Doping of the UCNP with rare-earth ions can tune their optical properties across the wavelength range from UV to the NIR.[1c,3] The UCNP are typically synthesized using high-temperature solvents methods to produce high crystallinity monodispersed nanoparticles.[4] Of particular interests are $NaYbF_4$ UCNPs which have enhanced optical efficiency (6× increase in absorption cross section[5]) due to high sensitizer $Yb^{3+}$ concentration in the host matrix compared to traditional $NaYF_4$.[6]

The UCNPs can be crystallized into different phases – cubic ($\alpha$ phase) and hexagonal ($\beta$ phase).[7] Hexagonal phase is considered advantageous for orders of magnitude enhancement of upconverting efficiency compared to the cubic phase.[8] However, the energy barrier of forming hexagonal $NaYbF_4$ UCNPs is much higher than the cubic phase, hence mostly small cubic crystal are reported.[4a,9] Previous work showed that the phase transition from cubic phase to hexagonal phase of UCNPs was a disordered to ordered process.[10] Typically in the cubic phase crystal cell, $Na^+$ and $Ln^{3+}$ are randomly distributed in the cationic sublattice. In the hexagonal crystal, the cation sites form three types, with a onefold fully occupied by the $Ln^{3+}$, another onefold randomly occupied by $Na^+$ and $Ln^{3+}$, and the twofold site with randomly distributed with $Na^+$ and vacancies.[4a,7b,10b,11] Ostwald-ripening the cubic phase crystal was successfully implemented to obtain small size hexagonal $NaYF_4$,[12] and the hexagonal crystals could be achieved using high temperature and long reaction time condition, where the ratio of $Na^+/Ln^{3+}$ in the cubic cell can be tuned.[7b,13] Moreover, manipulating the local structure in $\alpha$ phase by ion doping and ligands assisting method have been an useful tool to improve the phase transformation[7b,14] and to modify the emission properties.[15] However, it remains challenging to control the $NaYbF_4$ morphology and crystal phase, due to lack of direct experimental evidence and limited understanding of the mechanism of underlying phase transition.

Hence, we report a one pot synthesis of hexagonal $NaYbF_4$ UCNPs with controllable size and morphology by tuning the ratio of $Na^+/Yb^{3+}$ while keeping other reaction parameters constant.

W. Xiao, J. Chen, W. Luan, Y. Wu
CPCIF Key Laboratory of Advanced Battery Systems and Safety
School of Mechanical and Power Engineering
East China University of Science and Technology
Shanghai 200237, China
E-mail: luan@ecust.edu.cn

W. Xiao, F. Wang, L. Turyanska
Centre for Additive Manufacturing
Faculty of Engineering
University of Nottingham
Jubilee Campus, Nottingham NG8 1BB, UK
E-mail: lyudmila.turyanska@nottingham.ac.uk

The ORCID identification number(s) for the author(s) of this article can be found under https://doi.org/10.1002/adom.202303132



**DOI: 10.1002/adom.202303132**

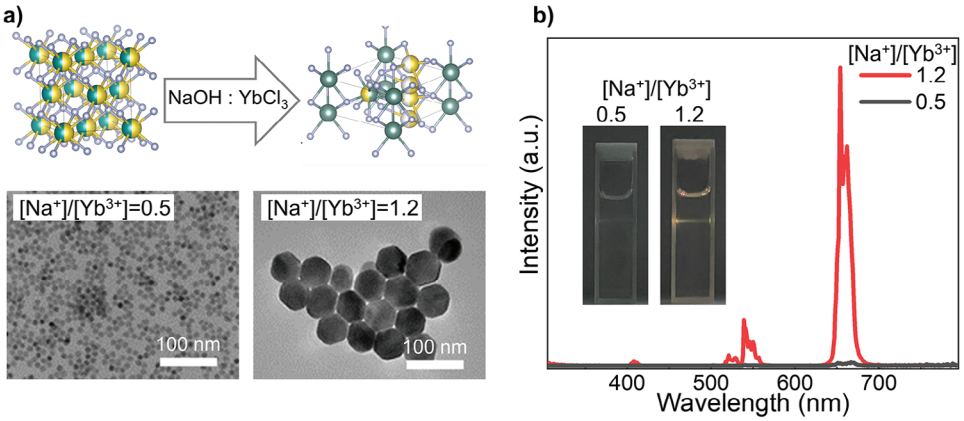


**Figure 1.** a) Scheme of the transformation of $NaYbF_4$ nanoparticles from cubic phase to hexagonal phase with increasing $[Na^+]/[Yb^{3+}]$. b) Room temperature PL spectrum of representative $NaYbF_4$: 2% $Er^{3+}$ synthesized with molar ratio $[Na^+]/[Yb^{3+}] = 0.5$ and 1.2, and (Inset) corresponding TEM images and images of the fluorescence of $NaYbF_4$: 2% $Er^{3+}$ solution under illumination with 980 nm.

By increasing the amount of NaOH used in the synthesis, we observed an aggregation of small cubic crystals induced phase transformation process with increased ratio of $Na^+/Yb^{3+}$ in the cubic cell. First principal calculation based on Density Functional Theory (DFT) was performed to study the trends of evolution of system energy, and revealed that local structure distortion and phonon dispersion happened while increasing the ratio of $Na^+/Yb^{3+}$ in the cubic cell and hence facilitated the formation of hexagonal crystal. Finally, we proposed a lattice strain-induced phase transformation mechanism driven by the cationic rearrangement and dislocation in local structure of cubic phase cell, which can be controlled by tuning the amount of sodium source used in synthesis.

## 2. Results and Discussion

### 2.1. Experimental Study of $NaYbF_4$: 2%$Er^{3+}$

The $NaYbF_4$ nanocrystals were synthesized following the modified process developed in the refs. [4b, 16]. Briefly, 1 mmol Ln-precursors were used with 10 ml oleic acid (OA), 15 ml 1-octadecene (ODE), and excess amount of $NH_4F$, with reaction taking under 315 °C for 60 min. We note, that the excess amount of $F^-$ precursor (8 mmol $NH_4F$) was used to eliminate the effect of $F^-$ content on crystal formation and growth. Phase transformation from spherical cubic-phase crystal to well-defined hexagonal crystal was fully achieved by increasing the molar ratio of $Na^+$ precursor and $Yb^{3+}$ precursor, $[Na^+]/[Yb^{3+}]$: cubic phase nanoparticles with $d_{NC} = 10.9 \pm 0.8$ nm are formed with from $[Na^+]/[Yb^{3+}] = 0.5$, while hexagonal nanoparticles with $d_{NC} = 50.6 \pm 10.0$ nm are formed with $[Na^+]/[Yb^{3+}] = 1.2$ (**Figure 1a**). The increase of the nanoparticle size was accompanied by significant (over 100 times) enhancement of photoluminescence (PL) intensity at 655 nm under excitation with $\lambda_{ex} = 980$ nm (Figure 1b). To explore the effect of $Na^+$ concentration on the formation of the nanocrystals, we performed the synthesis with the ratio of $[Na^+]/[Yb^{3+}]$ from 0.5 to 8.0. Transmission Electron Microscopy (TEM) imaging revealed that with increasing $Na^+$-content the average size of nanocrystal increased from $d_{NC} = 10.9 \pm 0.8$ nm to $82.1 \pm 8.1$ nm accompanied by shape evolution for the samples prepared with 0.5 mmol and 8 mmol of NaOH, respectively (**Figure 2**; Figure S2, Supporting Information).

The nanocrystals synthesized with low stoichiometric ratio of NaOH below 1.0 mmol had spherical shape (Figure 2a) with spacing of the crystal facets of 0.31 nm, corresponding to the (111)-plane of $NaYbF_4$ cubic phase (Figure S1a, Supporting Information). With increased $[Na^+]/[Yb^{3+}]$, the phase transition process occurred. For samples synthesized with $[Na^+]/[Yb^{3+}] = 1.0$, bimodal side distribution was observed (Figure 2b). Larger particles formed with size distribution $d_{NC} = 142.7 \pm 3.1$ nm and crystal plane separation of 0.55 nm (Figure S1c, Supporting Information), corresponding to the (100)-plane of hexagonal phase of $\beta$-$NaYbF_4$. In contrast, the smaller aggregated cluster had $d_{NC} = 34.1 \pm 1.2$ nm (Figure 2b) with the crystal spacing of 0.34 nm (Figure S1b, Supporting Information), corresponding to (111) plane of $\alpha$-$NaYbF_4$. A small number of aggregated cubic particles with $d_{NC} = 13.1 \pm 1.2$ nm (Figure S2c, Supporting Information) were observed, suggesting that the aggregation and merging of the cubic nanoparticles can lead to phase transition from cubic to hexagonal phase nanocrystal with well-defined edges. With increasing ratio of $[Na^+]/[Yb^{3+}]$ aggregation of cubic particles was observed due to change in surface energy, and the cationic rearrangement process occurs, accompanied by the accumulation of the dislocation or mismatches in the small cubic crystal. This can lead to recrystallization into hexagonal nanoparticles (Figure 2b; Figure S1b,c, Supporting Information).

For the samples prepared with $[Na^+]/[Yb^{3+}] > 1.2$, only hexagonal-shaped particles were observed, with an increased average size and broadened size distribution with higher $Na^+$ content, which we attribute to Ostwald ripening facilitated by the change of the surface charge.[7c,12a,17] With further increase of molar ratio $[Na^+]/[Yb^{3+}] = 8.0$, only hexagonal nanoparticles were formed with $d_{NC} = 82.1 \pm 8.1$ nm (Figure 2c).

The evolution of the phase with increasing molar ratio of $[Na^+]/[Yb^{3+}]$ was confirmed with X-Ray Diffraction (XRD) studies (**Figure 3a**). For samples produced with $[Na^+]/[Yb^{3+}] < 0.8$, the XRD patterns revealed pure cubic phases, corresponding to the JCPSD standard card no. 77–2043. By increasing $[Na^+]/[Yb^{3+}]$ from 0.8 to 1.2, the intensity of characteristic XRD peaks for hexagonal phase (JCPDS standard card no. 27–1427) increased

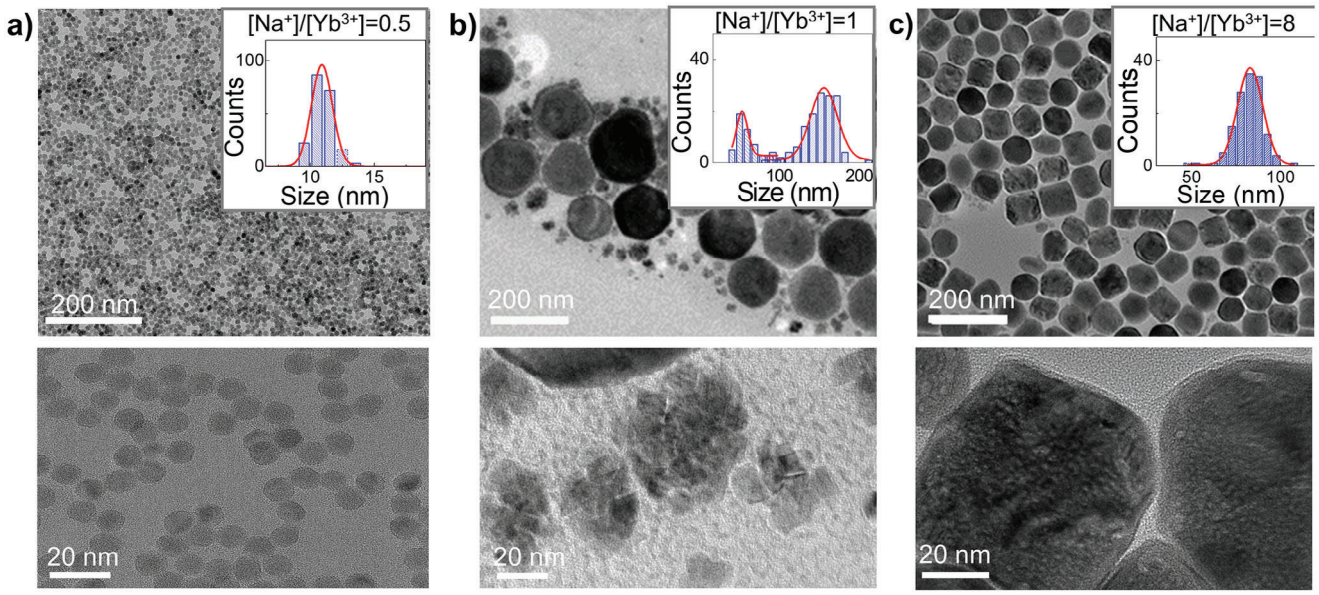


**Figure 2.** Representative TEM images and (insets) size distribution of the UCNPs synthesized with $[Na^+]/[Yb^{3+}]$ molar ratio of a) 0.5, b) 1.0, and c) 8.0.

and for the cubic phase gradually disappeared (Figure 3). Very weak signals of hexagonal crystal were observed for $[Na^+]/[Yb^{3+}] = 0.8$ and no detectable signals for cubic phase were observed for $[Na^+]/[Yb^{3+}] = 1.2$. Hence $0.8 \leq [Na^+]/[Yb^{3+}] < 1.2$ was assigned as the boundary for the phase transition. These results support the observation of a mixture of the aggregated cubic phase clusters and hexagonal crystals in our TEM studies (Figure 2b), confirming that the aggregation and merging of the cubic nanoparticles led to the phase transition from cubic to hexagonal (Figure 3b).

Interestingly, these main peaks of the XRD patterns of NPs prepared with $[Na^+]/[Yb^{3+}]$ from 0.5 to 1.0 shifted to smaller diffraction angles, suggesting that insufficient $Na^+$ content induced the lattice expansion rather than shrinkage of the crystal. We applied the Rietveld refinement to these XRD patterns (Figure S3, Supporting Information) and found that the

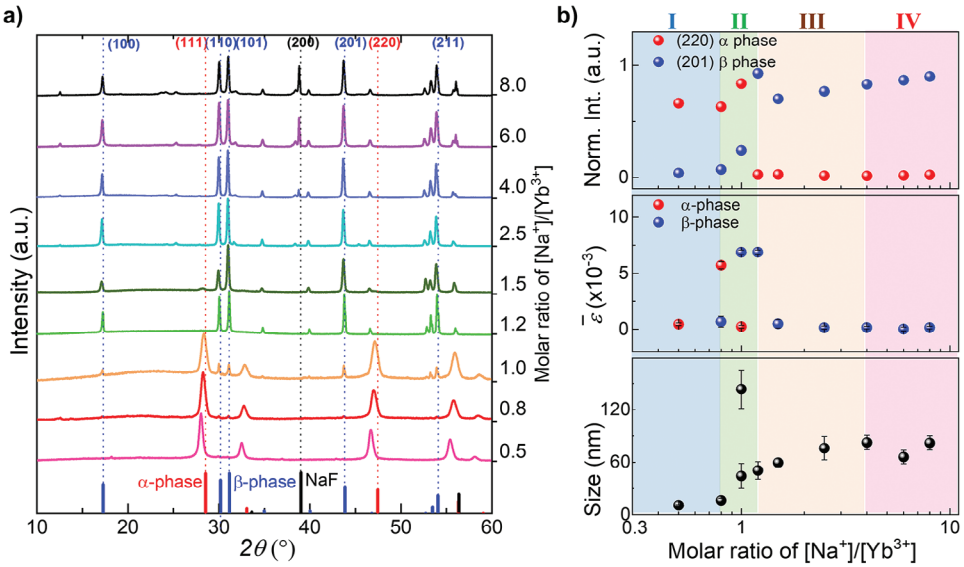


**Figure 3.** a) XRD patterns obtained for samples synthesized with molar ratio of $[Na^+]/[Yb^{3+}]$ from 0.5 to 8.0. JCPDS standard card for $\alpha$ phase, $\beta$ phase, and NaF are 77–2043, 27–1427, and 73–1922, respectively. b) Top: Normalized intensity of (220) peak of $\alpha$ phase and (201) peak of $\beta$ phase (top), the lattice strain (centre), and the size distribution (bottom) dependence of molar ratio of $[Na^+]/[Yb^{3+}]$. The XRD peaks were normalized by highest peak intensity of corresponding XRD pattern and the lattice strains with corresponding standard errors were calculated from the XRD patterns. Stage I (light blue): cubic phase for $[Na^+]/[Yb^{3+}] < 0.8$; Stage II (light green): phase transition from cubic to hexagonal within $0.8 \leq [Na^+]/[Yb^{3+}] < 1.2$; Stage III (light yellow): pure hexagonal phase within 1.2 to 4.0 of $[Na^+]/[Yb^{3+}]$. Stage IV(light purple): mixture phase of hexagonal phase and NaF by-product.

original cell length and cell volume decrease with increasing the $[Na^+]/[Yb^{3+}]$ from 0.5 to 1.0 (Table S1, Supporting Information): from 5.4802 Å to 5.4517 Å and from 164.58 $Å^3$ to 162.03 $Å^3$ for $[Na^+]/[Yb^{3+}] = 0.5$ and $[Na^+]/[Yb^{3+}] = 1$, respectively. In the lattice, $Na^+$ replaced the cation sites of $Yb^{3+}$ and led to the change of crystal phase, causing the lattice shrinkage due to change in the bond length, which we explored with DFT calculations, described below.

Deviation of the peaks from expected values decreased with increasing NaOH content. Thus, we attributed the observed changes in XRD patterns to the crystal lattice shrinkage from substitution of $Na^+$ (ion radius: 0.108 nm) to $Yb^{3+}$ (ion radius: 0.0858 nm).[18] To quantify the lattice strain, we apply Williamsone–Hall method[19b] in which the lattice strain is assumed to be uniform in all crystallographic directions. The broadening of XRD peak ($\beta_{hkl}$) can be calculated using the following equations:[19]

$$\beta_{hkl}\cos\theta = 4\varepsilon\sin\theta + \frac{k\lambda}{D} \quad (1)$$

where $D$ is the crystallite size domain, $k$ is the constant frequency, $\lambda$ is the wavelength, and $\theta$ is the diffraction angle.

Based on the W-H analysis, the lattice strain of $NaYbF_4$ (Figure 3b; Figure S4, Supporting Information) was found to be dependent on the molar ratio of $[Na^+]/[Yb^{3+}]$: in the phase transition stage, $0.5 < [Na^+]/[Yb^{3+}] < 0.8$, the lattice strain of cubic crystal increases $(5.48 \pm 0.33)\times10^{-3}$ but the lattice strain of hexagonal crystal remained low with the value of $(6.85 \pm 4.87) \times 10^{-4}$. For the hexagonal crystals formed with $[Na^+]/[Yb^{3+}] = 1.0$ (Figure 2b), an increase of lattice strain is calculated ($(6.89 \pm 0.18) \times 10^{-3}$). We note, that the lower value of lattice strain of cubic crystal of $2.43 \times 10^{-4} \pm 1.23 \times 10^{-4}$ is due to the lattice strain release facilitated by their aggregation into clusters. When the phase transition completed at $[Na^+]/[Yb^{3+}] = 1.2$, the lattice strain of hexagonal crystal remains unchanged. These results confirm the lattice strain-induced phase transition resulting from the accumulation of the dislocation and mismatches of $Na^+$ and $Yb^{3+}$ caused by the cationic rearrangement process. Both, the XRD studies (Figure 3a) and size evolution (Figure 3b, bottom) suggested the aggregation of cubic crystals and formation of cluster is crucial step for the growth of hexagonal crystals.

For the particles produced with $[Na^+]/[Yb^{3+}] \geq 1.2$, pure hexagonal phase was observed (JCPSD standard card no. 27–1427). Excessive of NaOH content would not affect the position of the XRD peaks and resulted in formation of NaF (JCPSD standard card no. 73–1922) by-product. Hence, the phase transformation was a multi-stages process[20] based on the analysis of the XRD pattern and TEM results of $NaYbF_4$ (Figure 3b). We observed the formation of pure cubic phase for $[Na^+]/[Yb^{3+}] < 0.8$ (Figure 3b), which is different from the report on $NaGdF_4$ where the formation of $GdF_3$ was observed instead of the cubic $NaGdF_4$ at low $Na^+$ content.[21] For the nanocrystal synthesized with $[Na^+]/[Yb^{3+}] =$ 0.8 to 1.2 (Figure 3b), the phase transition with rapidly increasing size of nanoparticles was observed. This result was similar to the previous report,[22] where excess of $F^-$ supplied and high $[F^-]/[Yb^{3+}]$ resulted in low energy barrier required for the phase transformation.[22b] Pure hexagonal phase nanocrystals were synthesized with $1.2 < [Na^+]/[Yb^{3+}] < 4$ (Figure 3b). Further increase of $[Na^+]/[Yb^{3+}]$ ratio led to formation of the mixture of NaF crystal and hexagonal phases (Figure 3b). We noted that the phase transition was accompanied by an increase of the particles size, which was previously attributed to high growth speed of the hexagonal phase.[7b,23]

### 2.2. Upconversion Luminescence Studies of $NaYbF_4$: 2%$Er^{3+}$

The upconversion luminescence studies of the as-synthesized $NaYbF_4$ revealed characteristic emission, with main peaks centered at 655 and 540 nm for all nanoparticles, independent of Na-content (**Figure 4a**). The emissions can be assigned to $^2H_{11/2} \rightarrow {}^4I_{15/2}$ and $^4F_{9/2} \rightarrow {}^4I_{15/2}$ transition in $Er^{3+}$ (Figure S4, Supporting Information), respectively. The intensity of the PL peak was weakly affected by increasing $[Na^+]/[Yb^{3+}]$ up to 0.8, corresponding to the cubic phase crystals. At the phase transition stage ($[Na^+]/[Yb^{3+}]$ from 1.0 to 1.2), the PL intensity gradually increased, as expected for an increasing population of hexagonal crystals, which had a more asymmetric point and lower crystal field energy than the cubic phase crystal.[24] Interestingly, a decrease of PL intensity was observed when the phase transformation was completed at $[Na^+]/[Yb^{3+}] = 1.5$, which can be attributed to the increased lattice strain in hexagonal crystal (Figure 3b), similar to that reported for $CsPbBr_3$ microwires.[25] We also note that the larger hexagonal nanoparticles are formed on expense of small cubic nanoparticles, hence overall number of particles decreases, contributing to the decrease of PL intensity.A significant enhancement of the PL intensity was recorded for higher $[Na^+]/[Yb^{3+}] = 4$, which can be explained by the growth of pure hexagonal crystals (Figure 4b). We observed a ≈20 times increase of PL integrated intensity for the nanoparticles produced with $[Na^+]/[Yb^{3+}] = 4.0$ compared to the sample with $[Na^+]/[Yb^{3+}] =$ 1.0, where the phase transition was observed, and a ≈610 times increase compared to the pure cubic phase UCNPs produced by $[Na^+]/[Yb^{3+}] = 0.5$.

Further increase of NaOH (>4 mmol) resulted in a decrease of PL intensity due to formation of NaF by-product, as revealed by the XRD studies. Combined ICP-AES results (Figure 4b) confirmed that with increasing Na-contents during synthesis, the incorporation of $Na^+$ into the crystals increased. For the pure cubic phase crystal (Stage I) and the phase transition stage (Stage II), the ratio of $[Na^+]/[Yb^{3+}]$ was smaller or equal to the theoretical value of 1.[12a] For hexagonal crystals, the actual $[Na^+]/[Yb^{3+}]$ ratio was over two times greater than the theoretical value. Hence, the accumulation of $Na^+$ is a key trigger of the phase transition process. The ICP-AES results also suggested that solid solution structure of $NaYbF_4$ crystal cell.[26]

### 2.3. First Principal Studies of $NaYbF_4$: 2%$Er^{3+}$

To explain the role of $Na^+$ in formation of hexagonal phase $NaYbF_4$ UCNPs, we performed first principal calculations based on the DFT. We built 2 × 2 × 1 supercell models (Figure S5, Supporting Information, 10.83 × 10.83 × 5.415 $Å^3$, 48 atoms) based on the fm-3m (225) space group oriented from the Inorganic Crystal Structure Database (ICSD) with the Collection Code 60258[27] to simulate the random distribution in the cationic sites.

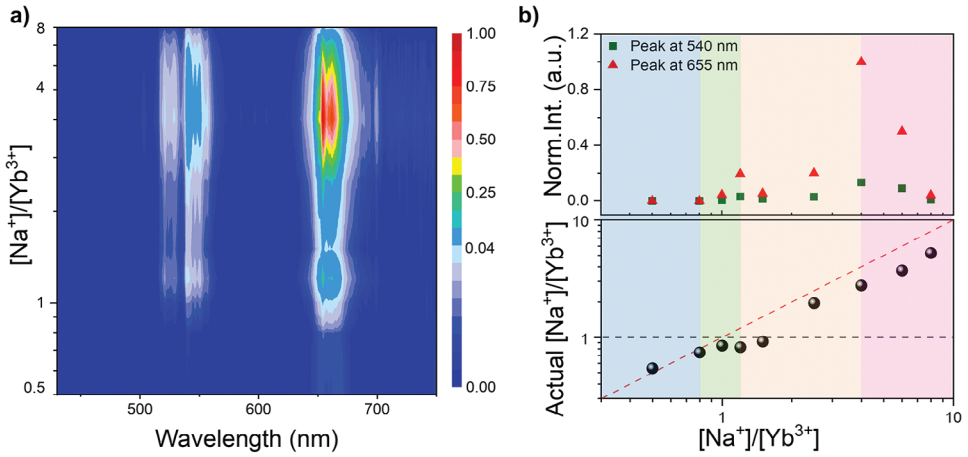


**Figure 4.** a) Photoluminescence (PL) emission spectra of 0.5–8.0 mmol as-synthesized $NaYbF_4$ samples and excited at 980 nm. The peak intensity was first normalized with the concentration of the $NaYbF_4$ cyclohexane solution and then normalized to maximum emission at 655 nm of $[Na^+]/[Yb^{3+}]$ = 4 sample. The spectra showed two main emission peaks at 540 nm (green) and 655 nm (red), where the emission can be assigned to $^2H_{11/2} \rightarrow {}^4I_{15/2}$ and $^4F_{9/2} \rightarrow {}^4I_{15/2}$ transition in $Er^{3+}$. b) Dependence of PL intensity (top) and actual $[Na^+]/[Yb^{3+}]$ measured by ICP-AES (bottom) on molar ratio of $[Na^+]/[Yb^{3+}]$ used in the synthesis. The black and red dash lines represent the theoretical $[Na^+]/[Yb^{3+}]$ values for $NaYbF_4$ and theoretical ICP results, respectively.

To investigate the trends of the influence of increasing $[Na^+]$ in the crystal cell, we revised the atomic fraction $[Na^+]$ in cationic sites in supercell models from 50% to 12.5%, 25%, 37.5% and 50%. And the possible arrangements of $Na^+$ and $Yb^{3+}$ in different $[Na^+]$ contents supercell models were calculated and settled by a script based on the StatisticalDisorder function in CASTEP. Three different $[Na^+]/[Yb^{3+}]$ distribution configurations of Na-50% supercell models were chosen to repeat calculation. All the supercell models were geometry optimized and fully relaxed to minimize the energy of models for the further calculations (Table S2, Supporting Information).

The dislocation of $Na^+$ and $Yb^{3+}$ in fully relaxed supercell models was observed when increasing the content of $Na^+$ from 12.5% to 50% (**Figure 5**a; Figure S6, Supporting Information), which confirmed the cations distribution induced accumulation of lattice distortion and lattice strain. To quantify the distortion among different atoms, the bond lengths of Na–F and its first nearest neighbor (1NN) and second nearest neighbor (2NN) Yb-F were calculated (Figure 5b). With increasing the content of $Na^+$ in the crystal, the average bond length of Na-F increased by only 0.5% and Yb-F decreased by 3%, which indicated the lattice strain were dominated by the shrinkage of the Yb-F and the stretch of the Na-F. The increased lattice distortion confirmed phase transformation process was dependent on the content of $Na^+$, with lattice strain accumulation and cationic rearrangement being the two main process.

Then we calculated the formation energy ($E_f$) of each model, which was defined as the energy difference per unit cell between

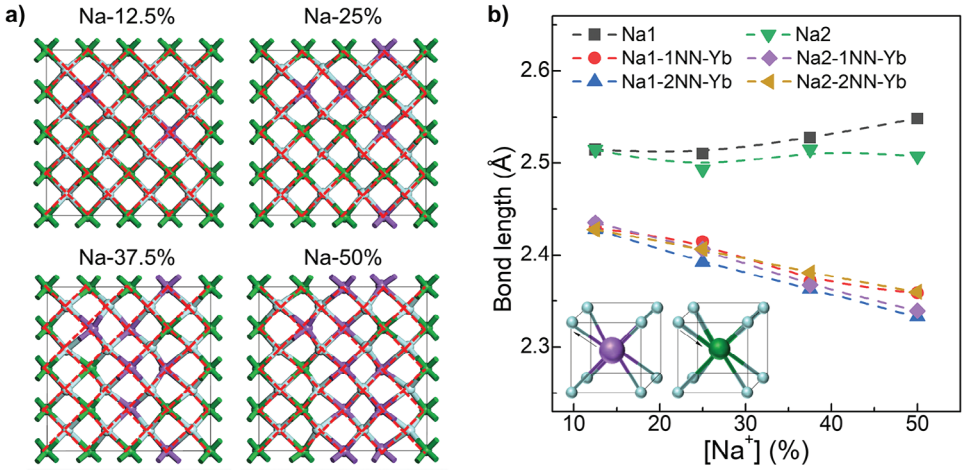


**Figure 5.** a) Scheme of lattice distortion in fully relaxed 2 × 2 × 1 $\alpha$-$NaYbF_4$ supercell theoretical model (Configuration 2) with 12.5%, 25%, 37.5%, 50% of $Na^+$ content. In which red dashed meshes represent the theoretical lattice of cell, purple balls, green balls, and light bule balls represent the sodium atoms, ytterbium atoms, and fluorine atoms, respectively. b) Calculated average Na-F and Yb-F bond lengths of first nearest neighbor and second nearest neighbor site of Na1 and Na2 for samples with different $Na^+$ content in $\alpha$-$NaYbF_4$ cell. Inset: scheme of $Na^+$ and $Yb^{3+}$ surrounded with eight $F^-$.

**Table 1.** Formation energy of different $Na^+$ content models.

| Model | Na-12.5% | Na-25% | Na-37.5% | Na-50% |
|---|---|---|---|---|
| Formula | $Na_2Yb_{14}$ | $Na_4Yb_{12}$ | $Na_6Yb_{10}$ | $Na_8Yb_8$ |
| $E_{total}$ (eV) | −113 414.2 | −103 233.1 | −93 046.3 | −82 851.7 |
| $E_f$(eV/atom) | −6.09 | −5.99 | −5.76 | −5.38 |

the nanocrystal and the isolated atoms.[7b,28] Hence, the $E_f$ was given by

$$E_f = \left[E_{total} - \left(16xE_{Na} + 16\left(1-x\right)E_{Yb} + 32E_F\right)\right]/N \quad (2)$$

where $x$ is the percentage of $[Na^+]$ in the supercell, $N$ is number of the atoms in the model and $N = 48$, $E_{Na} = -1302.3$ eV, $E_{Yb} = -6390.$ eV and $E_F = -657.9$ eV represented the atomic energies of isolated Na, Yb, and F given by the pseudo atomic calculation, and $E_{total}$ was the energy of the crystal cell.

The value of $E_f$ indicated the stability of the system. As shown in the **Table 1**, $E_f$ increased 0.71 eV/atom from 12.5% to 50% of $[Na^+]$. This increase of formation energy corresponded to the increase of $Na^+$ content in the cubic phase $NaYbF_4$ cell, which confirmed that the system had become unstable with increasing $[Na^+]/[Yb^{3+}]$ ratio. When the actual $[Na^+]$ in the cell reaches 50%, in agreement with the theoretical value, the formation energy reached the highest level and becomes most unstable. This was when the phase transition process started. Our DFT calculation demonstrated that high content of $[Na^+]$ led to the instability of the cubic phase, which was consistent with previously reports where the crystals formed with excess of $F^-$ lead to $\beta$ phase seeds generation.[29]

To confirm the influence of the increasing content of $Na^+$ on the dynamical phase stability of cubic cell, we performed the phonon dispersion and density of phonon states calculations (Figure S7, Supporting Information) along the high symmetry directions. 144 vibrational phonon modes for each supercell model were observed in acoustic branches (lied in low frequencies region) but none in the optical branches, which emerged from the concerted vibration of atoms in a lattice beyond their balancing position.[30] We note that optical properties of UCNPs originate from the photon transition of 4f electrons in lanthanide atoms rather than the vibration of the lattice. And there was no evidence of the out-of-phase oscillations of atoms in a lattice in Raman spectra investigation.[31] The maximum phonon energy increased from 349 $cm^{-1}$ for Na-12.5% model to 434 $cm^{-1}$ for Na-50% model, which implied that the system possessed higher vibration frequency with increased $Na^+$ content. (Figure S7, Supporting Information). We note that the imaginary phonon vibration mode (negative frequency value in phonon dispersion plots) appeared and increased with increased $Na^+$ content. The negative vibration states indicated that the system became less stable and phase transformation facilitated due to the potential breaking of atomic bonds and loss of crystal bonding energy.[28b,32]

## 3. Conclusion

In this work we successfully obtained the controllable size and morphology $NaYbF_4$: 2%$Er^{3+}$ by varying the molar ratio of $[Na^+]/[Yb^{3+}]$ used in synthesis. The mechanism of phase transformation from cubic to hexagonal was investigated by the experimental analysis and DFT simulation. Our results showed the nucleation and growth of hexagonal $NaYbF_4$ proceeded in four stages. For the first stage only small-size cubic nanoparticle can be obtained when limited sodium source was used. Phase transformation was successfully achieved in second stages by adjusting $[Na^+]/[Yb^{3+}]$ to 1.0, in which the aggregation of small cubic phase crystal and bimodal distribution was observed. The hexagonal crystal formed with promoting the content of sodium in third stage and upconversion emission was boosted. Further increase the $[Na^+]/[Yb^{3+}]$ above 4.0 in the fourth stage will induce the extraction of NaF and the loss of photoluminescence. Lattice strain-related phase transformation mechanism was proposed, which the phase transformation was triggered by the lattice strain due to the increasing dislocation of sodium and ytterbium ions with increasing content of sodium. Our work gives a new insight of phase controllable synthesis of $NaYbF_4$ and paves the way for applications of $NaYbF_4$ for biosensing, lighting, and more.

## 4. Experimental Section

*Materials*: Ytterbium (III) chloride hexahydrate ($YbCl_3{\cdot}6H_2O$, 99.9%), erbium (III) chloride hydrate ($YbCl_3{\cdot}6H_2O$, 99.9%), oleic acid (OA, 90%) and 1-octadecene (ODE, 90%) were purchased from Sigma Aldrich. Ammonium fluoride ($NH_4F$, ≥98%) and sodium hydroxide (NaOH) were purchased from General Reagent, and hexane, methanol, and ethanol were purchased from Adams. All chemicals were used as received without further purification.

*Synthesis of $NaYbF_4$:2%$Er^{3+}$*: The synthesis of $NaYbF_4$: 2% $Er^{3+}$ nanoparticles wercon method.[4b,27a] Briefly, 379.8 mg of $YbCl_3{\cdot}6H_2O$ (0.98 mmol) and 7.6 mmol $ErCl_3{\cdot}6H_2O$ (0.02 mmol) solid were combined with 10 ml oleic acid (OA) and 20 ml 1-octadecene (ODE) in a 100 ml three neck round bottom flask. The solution was stirred under Ar atmosphere at temperature $T = 160$°C for 1 h. After cooling to 50 °C, 5 ml NaOH (0.5 M) methanol solution and 16 ml $NH_4F$ (0.5 M) methanol solution were added dropwise into the flask and stirred for 1 h until the solution got clear. Then the solution was degassed at $T = 110$ °C for 15 min to remove the residual oxygen, water, and methanol. The solution was then heated to 315 °C for 1 h under continuous stiring. After cooling to room temperature, the nanoparticles were precipitated by ethanol, and collected by centrifugation at 6000 rpm for 10 min and washed three times with hexane/ethanol (v/v: 1/4) solution and centrifugation. The final product was dried and collected powder was stored at room temperature in atmosphere.

*DFT Simulations*: All the DFT calculations were performed using the CASTEP program on the BIOVIA MATERIALS STUDIO 2020 (Accelrys, Inc.). All the structure models were built and shown via VESTA program. During the calculations, the general gradient approximation (GGA) combined Perdew–Bruke–Ernzerhof function (PBE) was chosen for describing the exchange-correlation effects and electron interactions. And the ultrasoft pseudopotentials (USPP) were utilized to describe ion cores and valence electrons interactions. The valence electron configurations of F, Yb, and Na used for pseudo atomic calculation were $2s^2\ 2p^5$, $4f^{14}\ 5s^2\ 5p^6\ 6s^2$ and $2s^2\ 2p^6\ 3s^1$, respectively. The Ensemble DFT (EDFT) method was chosen as the electronic minimizer. For the geometry optimization, Broyden–Fletcher–Goldfarb–Shanno (BFGS) algorithm was used, and the convergence tolerance of energy, maximum force, maximum stress, and maximum displacement were selected as 2,0e-5 eV $atom^{-1}$, 0.05 eV $Å^{-1}$, 0.1 GPa, and 0.002 Å, respectively. The kinetic energy cut-off was chosen as 350 eV in the plane wave basis. For the self-consistent field (SCF) convergence, the SCF tolerance and the Monkhorst–Pack grid were set as 1.0e-6 eV $atom^{-1}$ and $1\times1\times2$, respectively. The phonon dispersion calculation

was carried out by finite displacement method using one 5 Å cutoff radius large supercell, and 0.015 $Å^{-1}$ was set as the q-vector separation.

*Characterization Methods*: Transmission electron microscopy (TEM) was carried on JEOL JEM 2100 Plus (Japan), *d*-spacing of the high-resolution images of nanoparticles were performed on Digital Micrograph, and size distribution was calculated using ImageJ. Powder XRD patterns were recorded on a Rigaku Ultimate IV powder X-ray Cu Ka radiation diffractometer (Japan) using Cu K$\alpha$ radiation ($\lambda = 0.1548$ nm). The elemental quantity analysis was carried out via inductively coupled plasma atomic emission spectroscopy (ICP-AES). The photoluminescence spectra were recorded by Edinburgh FLS 1000 with excitation provided by 980 nm continuous laser diode (MDL-III-2W, China).

## Supporting Information

Supporting Information is available from the Wiley Online Library or from the author.

## Acknowledgements

W.X. and J.C. contributed equally to this work. The authors gratefully acknowledge the support from the National Natural Science Foundation of China (52130511, 52375144), the China Scholarship Council, and the Engineering and Physical Sciences Research Council (grant number EP/P031684/1). The authors also acknowledge Dr. A. Foerster and Dr. S. Ghaderzadeh for the guidance and advice of DFT calculations.

## Conflict of Interest

The authors declare no conflict of interest.

## Data Availability Statement

The data that support the findings of this study are available from the corresponding author upon reasonable request.

## Keywords

density function theory (DFT), lattice strain, phase transformation, sodium, upconverting nanoparticles (UCNPs)

Received: December 8, 2023
Revised: January 17, 2024
Published online:

[1] a) C. Sun, M. Gradzielski, *Adv. Colloid. Interface. Sci.* **2022**, *300*, 102579; b) M. Haase, H. Schafer, *Angew Chem Int Ed Engl* **2011**, *50*, 5808; c) X. Zheng, R. K. Kankala, C. G. Liu, Y. Wen, S. B. Wang, A. Z. Chen, Y. Zhang, *Adv. Opt. Mater.* **2022**, *10*, 2200167.

[2] a) P. Peng, N. Wu, L. Ye, F. Jiang, W. Feng, F. Li, Y. Liu, M. Hong, *ACS Nano* **2020**, *14*, 16672; b) C. Hazra, A. Skripka, S. J. L. Ribeiro, F. Vetrone, *Adv. Opt. Mater.* **2020**, *8*, 2001178; c) C. Chen, C. Wu, J. Yu, X. Zhu, Y. Wu, J. Liu, Y. Zhang, *Coord. Chem. Rev.* **2022**, *461*, 214495; d) Z. Zhang, M. K. G. Jayakumar, X. Zheng, S. Shikha, Y. Zhang, A. Bansal, D. J. J. Poon, P. L. Chu, E. L. L. Yeo, M. L. K. Chua, S. K. Chee, Y. Zhang, *Nat. Commun.* **2019**, *10*, 4586.

[3] F. Wang, X. Liu, *J. Am. Chem. Soc.* **2008**, *130*, 5642.

[4] a) H.-X. Mai, Y.-W. Zhang, R. Si, Z.-G. Yan, L.-d. Sun, L.-P. You, C.-H. Yan, *J. Am. Chem. Soc.* **2006**, *128*, 6426; b) B. Chen, W. Kong, N. Wang, G. Zhu, F. Wang, *Chem. Mat.* **2019**, *31*, 4779.

[5] A. Schroter, S. Märkl, N. Weitzel, T. Hirsch, *Adv. Funct. Mater.* **2022**, *32*, 2113065.

[6] a) B. Tian, A. Fernandez-Bravo, H. Najafiaghdam, N. A. Torquato, M. V. P. Altoe, A. Teitelboim, C. A. Tajon, Y. Tian, N. J. Borys, E. S. Barnard, M. Anwar, E. M. Chan, P. J. Schuck, B. E. Cohen, *Nat. Commun.* **2018**, *9*, 3082; b) B. Chen, F. Wang, *Trends Chem.* **2020**, *2*, 427; c) J. Wang, R. Deng, M. A. MacDonald, B. Chen, J. Yuan, F. Wang, D. Chi, T. S. Hor, P. Zhang, G. Liu, Y. Han, X. Liu, *Nat. Mater.* **2014**, *13*, 157.

[7] a) M. Quintanilla, E. Hemmer, J. Marques-Hueso, S. Rohani, G. Lucchini, M. Wang, R. R. Zamani, V. Roddatis, A. Speghini, B. S. Richards, F. Vetrone, *Nanoscale* **2022**, *14*, 1492; b) F. Wang, Y. Han, C. S. Lim, Y. Lu, J. Wang, J. Xu, H. Chen, C. Zhang, M. Hong, X. Liu, *Nature* **2010**, *463*, 1061; c) N. J. Johnson, A. Korinek, C. Dong, F. C. van Veggel, *J. Am. Chem. Soc.* **2012**, *134*, 11068.

[8] a) H.-X. Mai, Y.-W. Zhang, L.-D. Sun, C.-H. Yan, *J. Phys. Chem. C* **2007**, *111*, 13730; b) F. Wang, X. Liu, *Chem. Soc. Rev.* **2009**, *38*, 976.

[9] J. Ren, G. Jia, Y. Guo, A. Wang, S. Xu, *J. Phys. Chem. C* **2015**, *120*, 1342.

[10] a) Y. Sui, K. Tao, Q. Tian, K. Sun, *J. Phys. Chem. C* **2012**, *116*, 1732; b) X. Zhai, Y. Wang, X. Liu, S. Liu, P. Lei, S. Yao, S. Song, L. Zhou, J. Feng, H. Zhang, *Chem. Photo. Chem.* **2017**, *1*, 369.

[11] A. Aebischer, M. Hostettler, J. Hauser, K. Kramer, T. Weber, H. U. Gudel, H. B. Burgi, *Angew. Chem., Int. Ed. Engl.* **2006**, *45*, 2802.

[12] a) T. Rinkel, J. Nordmann, A. N. Raj, M. Haase, *Nanoscale* **2014**, *6*, 14523; b) T. Rinkel, A. N. Raj, S. Duhnen, M. Haase, *Angew. Chem., Int. Ed. Engl.* **2016**, *55*, 1164.

[13] J. Zhao, B. Chen, X. Chen, X. Zhang, T. Sun, D. Su, F. Wang, *Nanoscale* **2020**, *12*, 13973.

[14] H. Na, K. Woo, K. Lim, H. S. Jang, *Nanoscale* **2013**, *5*, 4242.

[15] a) H. Dong, L. D. Sun, C. H. Yan, *J. Am. Chem. Soc.* **2021**, *143*, 20546; b) M. D. Wisser, M. Chea, Y. Lin, D. M. Wu, W. L. Mao, A. Salleo, J. A. Dionne, *Nano. Lett.* **2015**, *15*, 1891.

[16] F. Wang, R. Deng, X. Liu, *Nat. Protoc.* **2014**, *9*, 1634.

[17] M. Wang, Y. Zhang, Q. Yao, M. Ng, M. Lin, X. Li, K. K. Bhakoo, A. Y. Chang, F. Rosei, F. Vetrone, *Chem. Mat.* **2019**, *31*, 5160.

[18] a) S. Sinha, M. K. Mahata, H. C. Swart, A. Kumar, K. Kumar, *New J. Chem.* **2017**, *41*, 5362; b) S. Gai, C. Li, P. Yang, J. Lin, *Chem. Rev.* **2014**, *114*, 2343.

[19] a) S. Dolabella, A. Borzi, A. Dommann, A. Neels, *Small Methods* **2022**, *6*, 2100932; b) A. K. Zak, W. H. A. Majid, M. E. Abrishami, R. Yousefi, *Solid State Sci.* **2011**, *13*, 251.

[20] a) S. Radunz, A. Schavkan, S. Wahl, C. Würth, H. R. Tschiche, M. Krumrey, U. Resch-Genger, *J. Phys. Chem. C* **2018**, *122*, 28958; b) J. D. Suter II, N. J. Pekas, M. T. Berry, P. S. May, *J. Phys. Chem. C* **2014**, *118*, 13238.

[21] S. Dühnen, T. Rinkel, M. Haase, *Chem. Mat.* **2015**, *27*, 4033.

[22] a) E. Lu, J. Pichaandi, C. K. Rastogi, L. P. Arnett, M. A. Winnik, *Chem. Mat.* **2019**, *31*, 9742; b) R. Shi, X. Ling, X. Li, L. Zhang, M. Lu, X. Xie, L. Huang, W. Huang, *Nanoscale* **2017**, *9*, 13739.

[23] X. Chen, L. Jin, W. Kong, T. Sun, W. Zhang, X. Liu, J. Fan, S. F. Yu, F. Wang, *Nat. Commun.* **2016**, *7*, 10304.

[24] M. D. Wisser, S. Fischer, P. C. Maurer, N. D. Bronstein, S. Chu, A. P. Alivisatos, A. Salleo, J. A. Dionne, *ACS Photonics* **2016**, *3*, 1523.

[25] P. Ghosh, U. Farooq, H. Su, S. Pei, G. Li, W. He, J. Dai, L. Huang, M. Huang, *J. Mater. Sci.* **2022**, *57*, 5061.

[26] L. P. Otroshchenko, B. P. Sobolev, L. E. Fykina, A. A. Bystrova, *Crystallogr. Rep.* **2000**, *45*, 926.

[27] D. M. Roy, R. Roy, *J. Electrochem. Soc.* **1964**, *111*, 421.

[28] L. Yao, Y. Li, D. Xu, H. Lin, Y. Peng, S. Yang, Y. Zhang, *New J. Chem.* **2019**, *43*, 3848.

[29] a) X. Pan, J. Ren, J. Zeng, M. Liu, Z. Fang, Q. Ju, *Inorg. Chem. Front.* **2022**, *9*, 4081; b) C. K. Rastogi, E. Lu, J. Tam, J. M. Pichaandi, J. Howe, M. A. Winnik, *Langmuir* **2021**, *37*, 2146.

[30] a) A. Siddique, A. Khalil, B. S. Almutairi, M. Bilal Tahir, T. Ahsan, A. Hannan, H. Elhosiny Ali, H. Alrobei, M. Alzaid, *Chem. Phys.* **2023**, *568*, 111851; b) D. H. Moseley, R. Juneja, L. L. Daemen, I. Sergueev, R. Steinbrugge, O. Leupold, Y. Cheng, V. R. Cooper, L. Lindsay, M. K. Kidder, M. E. Manley, R. P. Hermann, *Inorg. Chem.* **2023**, *62*, 16464.

[31] J. F. Suyver, J. Grimm, M. K. van Veen, D. Biner, K. W. Krämer, H. U. Güdel, *J. Lumines.* **2006**, *117*, 1.

[32] G. Lefevre, A. Herfurth, H. Kohlmann, A. Sayede, T. Wylezich, S. Welinski, P. Duarte Vaz, S. F. Parker, J. F. Blach, P. Goldner, N. Kunkel, *J. Phys. Chem. C* **2018**, *122*, 10501.